PROGRESS IN PHOTOVOLTAICS: RESEARCH AND APPLICATIONS
Prog. Photovolt: Res. Appl. (2011)
Published online in Wiley Online Library (wileyonlinelibrary.com). DOI: 10.1002/pip.1082

RESEARCH ARTICLE

Interstitial iron concentrations across multicrystalline silicon wafers via photoluminescence imaging

AnYao Liu[1]*, Yang-Chieh Fan[1,2] and Daniel Macdonald[1]

[1] School of Engineering, College of Engineering and Computer Science, Australian National University, Canberra, ACT 0200, Australia
[2] Photovoltaics Centre of Excellence, The University of New South Wales, Sydney, New South Wales 2052, Australia

ABSTRACT

We present high-resolution images of the lateral distribution of interstitial iron across wafers from various positions along the length of a directionally solidified multicrystalline silicon ingot. Iron images were taken on wafers in the as-cut state and also after two different phosphorus gettering steps performed at 845°C for 30 min, one with an additional anneal at 600°C for 5 h (referred to as extended gettering). The iron images were obtained by taking calibrated photoluminescence (PL) images of the low injection carrier lifetimes, before and after dissociation of iron–boron pairs via strong illumination. The iron images clearly reveal the internal gettering of iron during ingot cooling to grain boundaries and dislocation clusters, resulting in much lower dissolved iron concentrations at those features. In contrast, the PL images of gettered wafers exhibit a reversed distribution of dissolved iron compared to the as-cut wafers, in other words, with higher interstitial iron concentrations at the grain boundaries than within the grains, most probably owing to the precipitated iron at the grain boundaries partly dissolving during the high-temperature gettering process. Phosphorus gettering was found to result in a significant reduction of interstitial iron both inside the grains and at grain boundaries. The extended gettering resulted in a further significant reduction in all parts of the wafers and along all sections of the ingot. Copyright © 2011 John Wiley & Sons, Ltd.

KEYWORDS

photoluminescence imaging; interstitial iron distribution; multicrystalline silicon; phosphorus gettering

***Correspondence**

AnYao Liu, School of Engineering, College of Engineering and Computer Science, Australian National University, Canberra, ACT 0200, Australia.
E-mail: u4393070@anu.edu.au

Received 26 August 2010; Revised 26 October 2010

1. INTRODUCTION

Iron is one of the most common metallic impurities in ingot-grown multicrystalline silicon (mc-Si) for solar cells, the presence of which significantly reduces the carrier lifetime in the 'as-cut' wafers [1]. It originates mostly from the crucible and crucible lining during ingot crystallisation [2]. The concentration of dissolved interstitial iron, $[Fe_i]$, is known to vary along the length of an ingot [1] and undergoes changes during cell processing due to iron precipitation, dissolution and impurity gettering. In order to better understand the behaviour of iron in mc-Si and thus to explore possible ways to mitigate its negative impacts, we study the distribution of interstitial iron across mc-Si wafers and along the length of an ingot in the as-cut state and also after phosphorus gettering steps. For this purpose, we have applied the recently developed technique of imaging interstitial iron concentrations using photoluminescence (PL) images taken before and after dissociation of FeB pairs [3].

2. EXPERIMENT

The samples used were wafers from different sections of a standard commercially grown p-type boron-doped 1.6 Ωcm (nominal) directionally solidified mc-Si ingot. The wafers were 12.5 cm × 12.5 cm in size and approximately 0.033 cm thick and numbered such that 1 denotes the bottom of the ingot, to approximately 370 at the top. Wafers from along the length of the ingot were alkaline etched and set aside as 'as-cut' wafers. Neighbouring wafers were alkaline etched and received a 30 min double

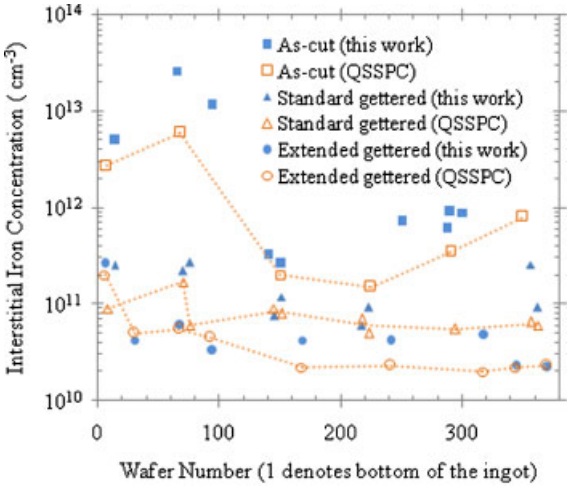

Figure 1. Average interstitial iron concentration of wafers from different sections of the ingot, measured in this work by PL imaging and previously by QSSPC. Lines are guides to the eye.

sided phosphorus diffusion at 845°C, resulting in diffusions of around 70 Ω/square on both sides. Some of these wafers received an additional anneal at 600°C for 5 h and these wafers are referred to as 'extended gettered', as opposed to 'standard gettered'. This additional anneal was performed *in situ* during cooling down from the gettering temperature. The gettering diffusions were then acid etched and the wafer surfaces were passivated with silicon nitride films deposited by plasma-enhanced chemical vapour deposition (PECVD).

The PL technique for imaging interstitial iron in silicon is detailed in Ref. [3]. Here we have assumed the same energy levels and capture cross-sections for Fe_i and FeB pairs as were used in that work. The PL imaging was performed with BTimaging LIS-R1, in which an 808 nm laser is used as the carrier generation source during lifetime imaging [4]. The interstitial iron images were achieved by taking calibrated PL images of the carrier lifetimes before and after dissociation of FeB pairs [5]. Pair dissociation was achieved via strong illumination with a photographic flash with a peak intensity of several 100 suns and a flash duration of 1/300 s to avoid sample heating, repeated between 10 and 20 times in quick succession. The

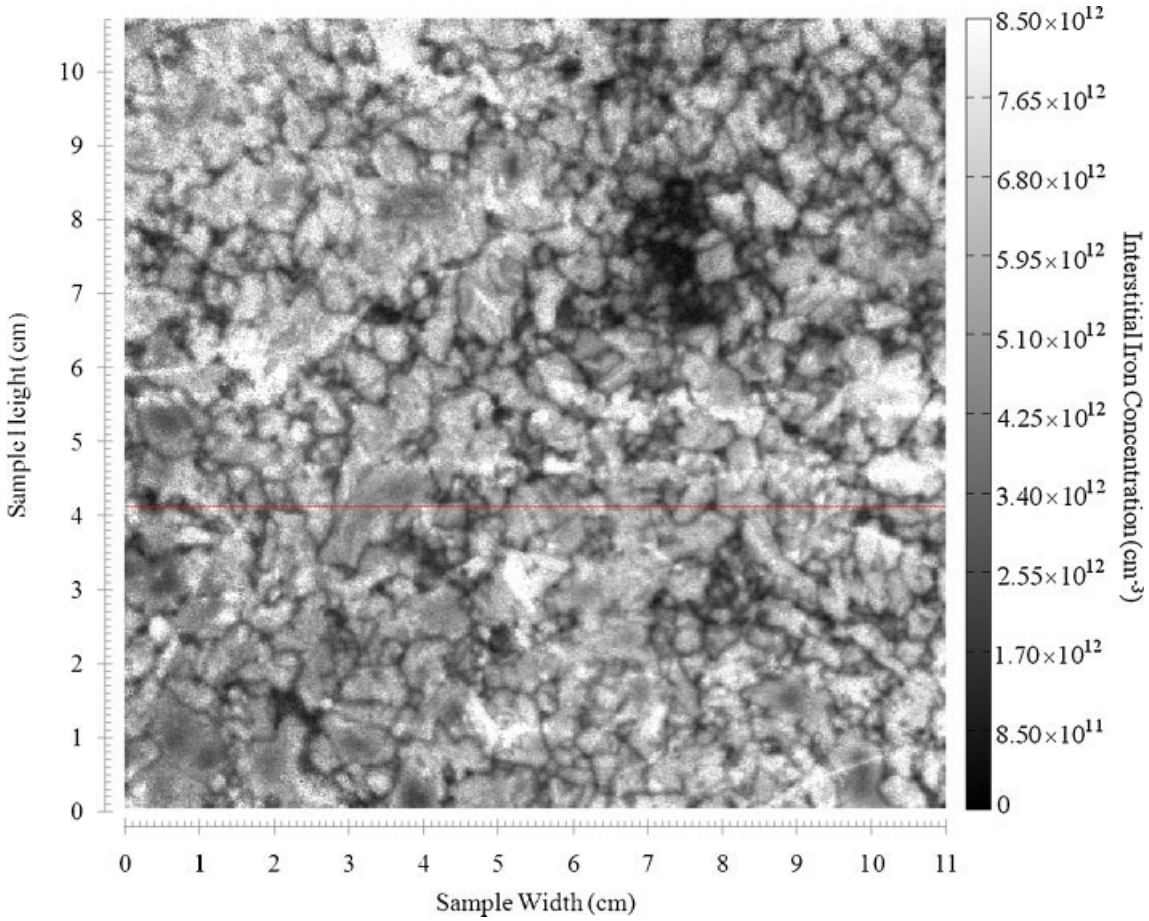

Figure 2. Interstitial iron image of as-cut wafer 13. The red line indicates the position of cross-section shown in Figure 6.

conversion factors for converting PL images into lifetime images were obtained via comparison with area-averaged lifetime measurements using the quasi-steady-state photoconductance (QSSPC) method [6], taken at high enough injection levels to avoid minority carrier trapping [7], but low enough to ensure the excess carrier density is well below the base doping and therefore leading to a linear relationship between the carrier lifetime and the PL intensity [8]. The actual carrier lifetime images then used for iron imaging were taken at lower injection levels, with excess carrier densities between 1×10^{12} and $2 \times 10^{13}\,\mathrm{cm}^{-3}$, which is well below the 'cross-over' point [9]. This approach has two distinct advantages. Firstly, the lower laser intensity (around 0.2–0.3 suns) during the lifetime imaging ensures an insignificant fraction of the FeB pairs are broken during the measurement itself. This results from the fact that the FeB pair breaking rate increases approximately quadratically with the laser intensity [10], while the exposure time required to obtain a clear image only decreases approximately linearly. Secondly, it has been shown that non-uniform carrier profiles in regions with very low lifetimes can distort the calculated iron concentrations [11]. However, in the true low-injection region, where the carrier lifetimes are independent of the injection level, such non-uniform profiles do not affect the determination of the lifetime and this artefact is avoided. This highlights an advantage of using PL imaging for determining iron concentrations, since other methods for measuring carrier lifetimes, such as the QSSPC method, are often not applicable in true low-injection conditions, due to the presence of trapping effects, for example [12].

To validate our technique, the wafer-averaged interstitial iron concentrations measured by PL imaging were compared to previous measurements [13] using the well-established QSSPC technique. In contrast to the PL images, the QSSPC carrier lifetime measurements were taken at an excess carrier density of $1 \times 10^{15}\,\mathrm{cm}^{-3}$, in order to avoid minority carrier trapping effects and to be well above the cross-over point. In addition, the QSSPC

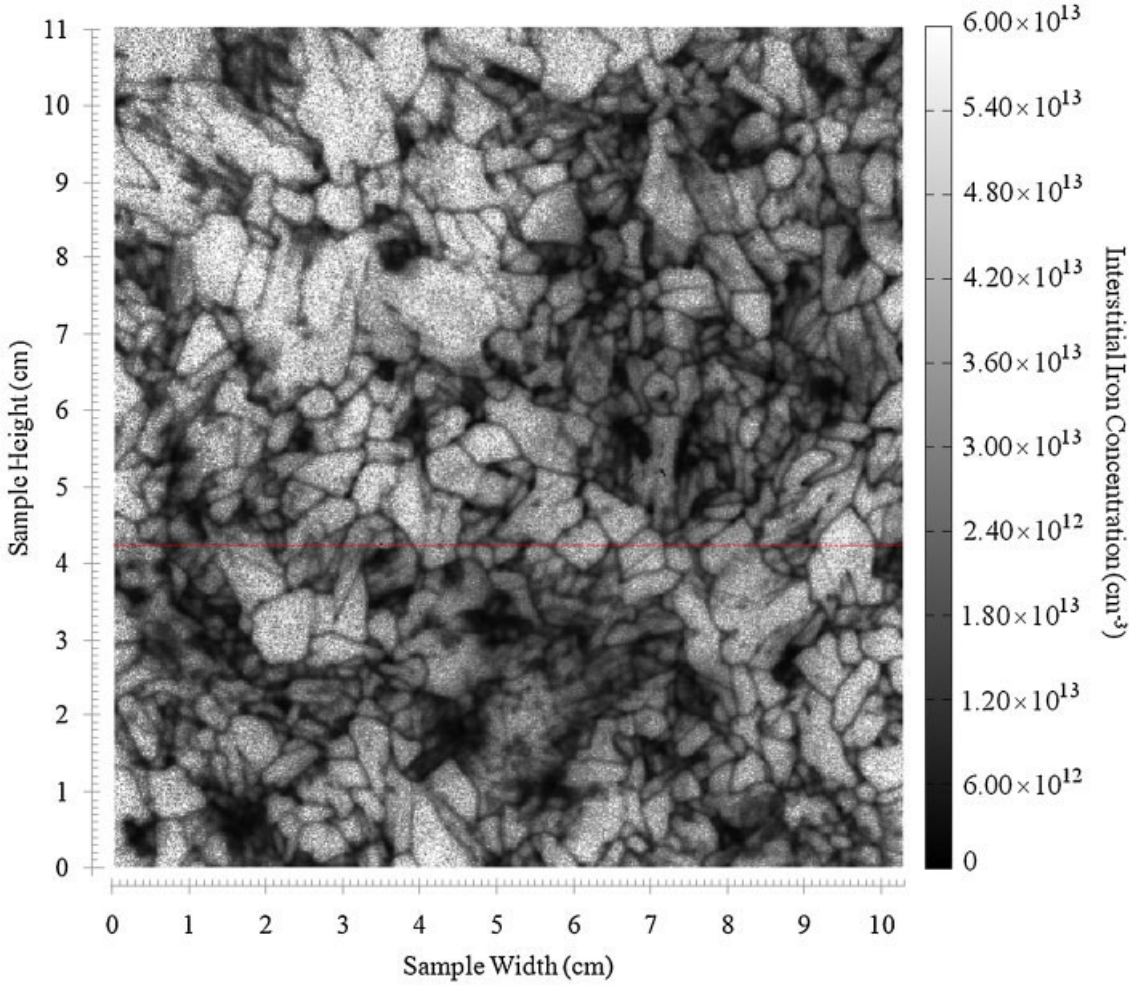

Figure 3. Interstitial iron image of as-cut wafer 65. The red line indicates the position of cross-section shown in Figure 6.

measurements covered an area of a few square centimetres and thus only represent a fraction of the area measured by PL imaging. FeB pair dissociation with QSSPC measurements was achieved by illumination of roughly 1 sun for 30–60 s. The interstitial iron concentration should of course be independent of the injection level and so the PL and QSSPC derived Fe concentrations should coincide, although some variation may be expected due to the smaller detection area of the QSSPC data.

3. RESULTS AND DISCUSSION

3.1. Technique Confirmation

Figure 1 shows a comparison of wafer-averaged [Fe_i] measured by PL imaging (this work) and previous QSSPC measurements [13]. The results obtained from these two techniques agree in general, which gives confidence in the PL technique for measuring [Fe_i] in mc-Si wafers at an injection level below the cross-over point. Note that although the QSSPC technique is also used to calibrate the PL images, this calibration is performed at a much higher injection level, around $10^{15}\,cm^{-3}$ and so the comparison of the low-injection iron images obtained by PL with the mid-injection average [Fe_i] values obtained by QSSPC is useful in demonstrating that the energy levels and capture cross-section values assumed are reasonable across this range of injection levels. However, it can be seen that our measurements of [Fe_i] are in some cases larger than those from QSSPC. We believe this does not reflect a deficiency in the PL imaging technique, but rather is due to a stronger illumination source used in this experiment to accomplish a more thorough dissociation of FeB pairs. Figure 1 also illustrates the lateral change in dissolved iron distribution along the length of the ingot, the discussion of which will be detailed in the following sections.

3.2. As-cut wafers

Figures 2–5 shows the interstitial iron images of as-cut wafers 13, 65, 94 and 140, taken from near the bottom through to the middle of the ingot. The size of the region shown is approximately 10.8 cm by 10.8 cm, with the actual sizes shown in the Figures 2–5. The grain boundaries are clearly evident in these images. For the as-cut wafers, the concentrations of interstitial iron at the grain boundaries are significantly less than inside the grains. This is caused by the precipitation of dissolved iron at grain boundaries during ingot growth. Regions of high-dislocation densities appear as extended dark regions (particularly in Figures 2 and 3) and evidently also act as strong precipitation sites for interstitial iron during ingot cooling. This phenomenon has been observed previously

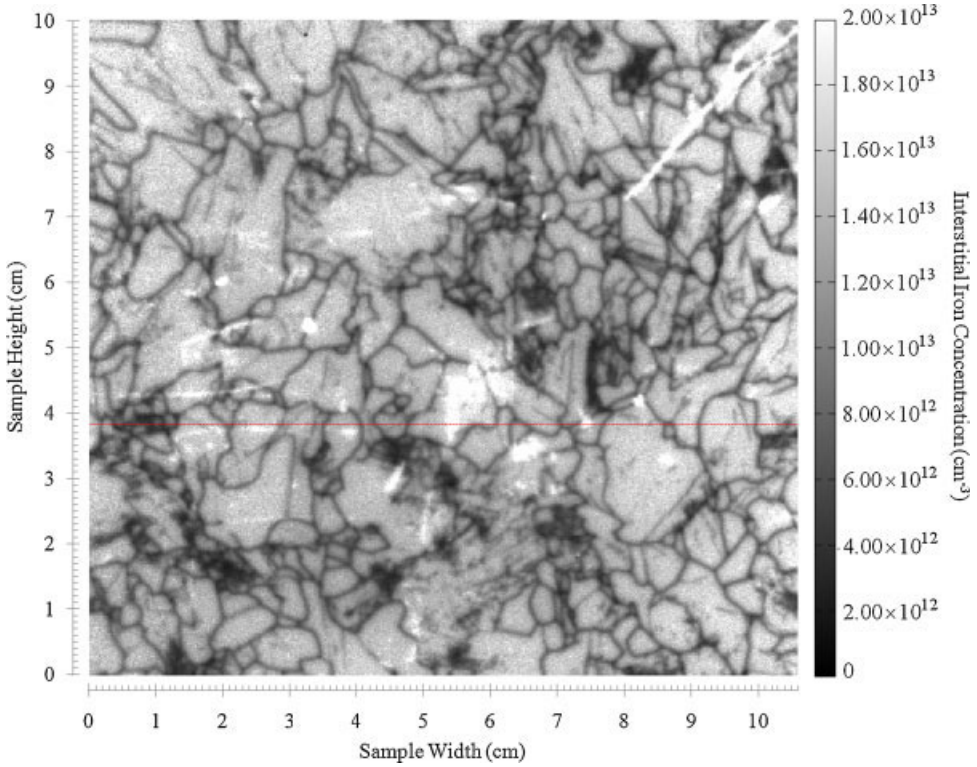

Figure 4. Interstitial iron image of as-cut wafer 94. The red line indicates the position of cross-section shown in Figure 6.

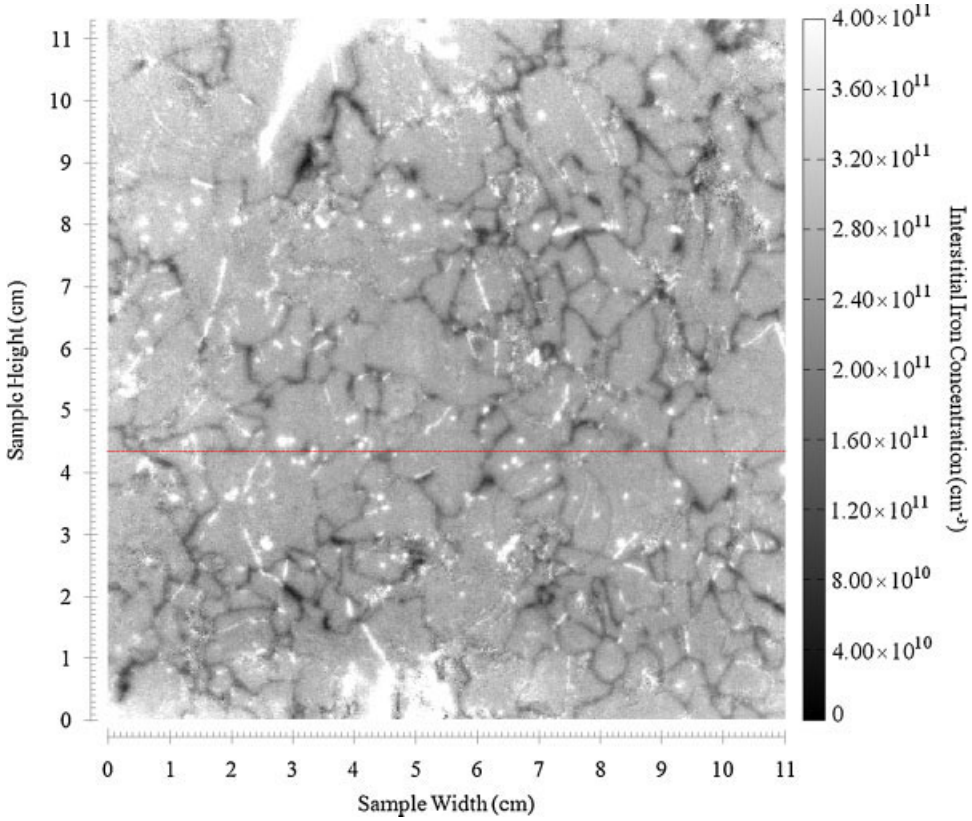

Figure 5. Interstitial iron image of as-cut wafer 140. The red line indicates the position of cross-section shown in Figure 6.

with other techniques [14–16] and also with PL-based iron imaging [3,17,18]. However, it is noteworthy that not all grain boundaries seem to act as strong precipitation sites for iron. In particular, twin boundaries inside the grains are not visible in any of the Fe_i images, despite being common under direct visual inspection of the wafers, implying that such twins do not act as precipitation sites for interstitial iron.

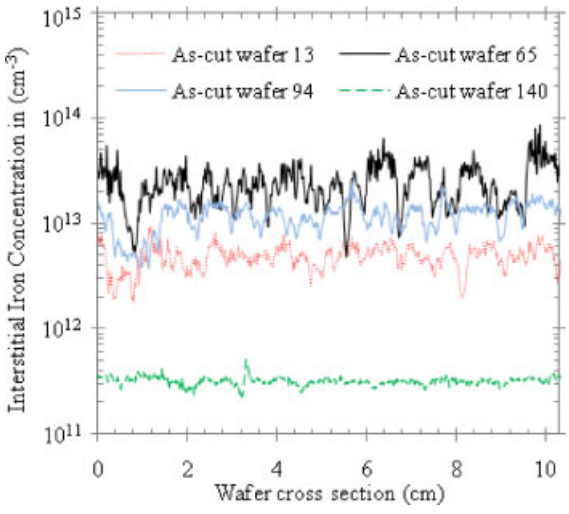

Figure 6. Interstitial iron concentrations of the cross-sections of as-cut wafers. The same position of cross-section is chosen for all wafers, as indicated by the red lines in Figures 2–5.

A quantitative representation of $[Fe_i]$ for the as-cut wafers is illustrated in Figure 6 in the form of cross-sections, taken at the position of the horizontal lines shown in Figures 2–5. The maximum $[Fe_i]$ within grains is shown to be quite uniform for a given wafer, possibly reflecting solubility-limited precipitation during ingot cooling. Another obvious feature is that the dissolved iron concentration is actually highest for wafer 65, rather than wafer 13 from nearer the bottom. This is surprising at first, considering that the iron diffuses from the bottom of the ingot during ingot growth. However, this trend has been observed previously [19]. The iron images presented here allow us to identify two mechanisms that contribute to this effect.

Firstly, it can be seen that the grain size increases moving up the ingot. At the very bottom of the ingot, as depicted by as-cut wafer 13 in Figure 2, the grains are of small size. This denotes the start of crystallisation. Moving up to as-cut wafer 65 in Figure 3, the grain structure is more evolved. The total length of grain boundaries per unit area therefore decreases due to enlarged grain sizes, hence resulting in fewer precipitation sites for dissolved iron at the grain boundaries.

Secondly, the dissolved iron concentrations *within* the grains are also higher in wafer 65, as shown in Figure 6.

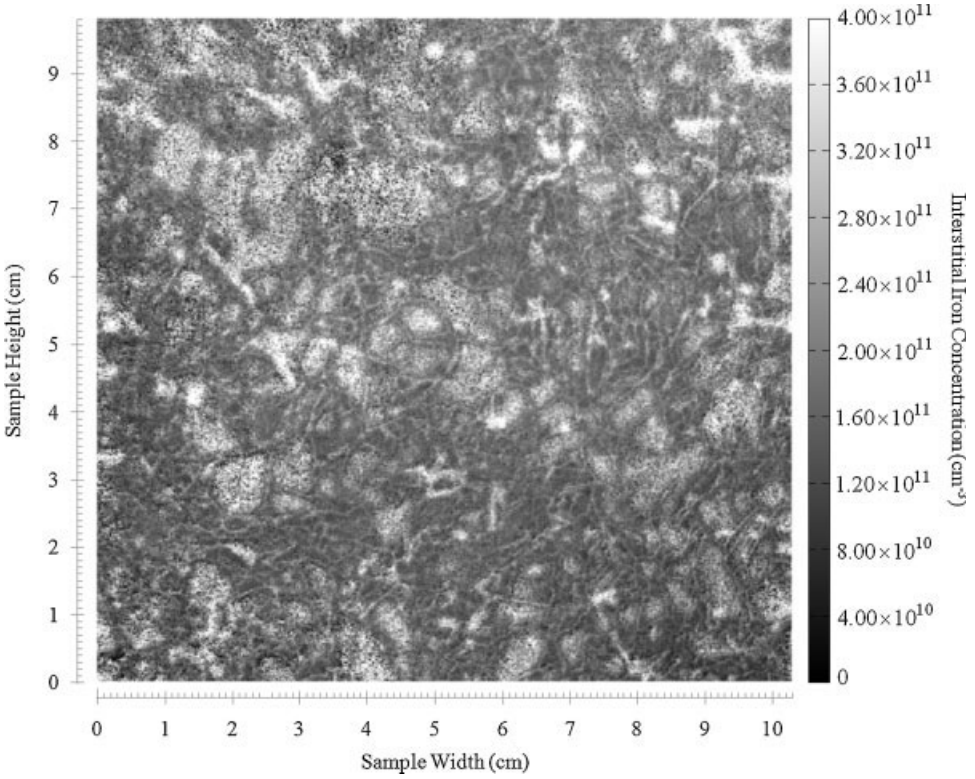

Figure 7. Interstitial iron image of standard gettered wafer 70.

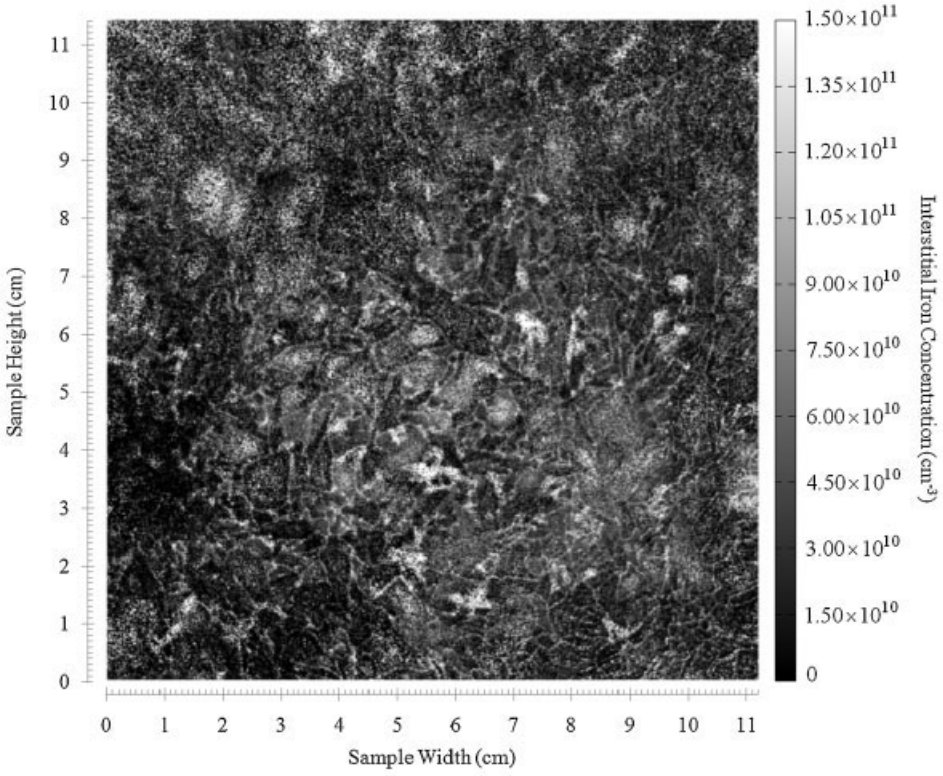

Figure 8. Interstitial iron image of extended gettered wafer 67.

This indicates that there are additional precipitation sites for Fe within the grains near the bottom of the ingot. We propose that these sites could be oxygen precipitates within the grains, which are more likely near the very bottom of ingots [20] and are known to act as precipitation sites for dissolved iron [21]. Alternatively, the effect could be caused by increased super-saturation of dissolved Fe due to in-diffusion from the crucible near the very bottom, triggering a greater degree of precipitation.

Even further up the ingot, as demonstrated by as-cut wafer 94 in Figure 4, [Fe_i] starts to decline again, both inside grains and at grain boundaries (see Figure 6). As the main source of iron in this part of the ingot is solid-state diffusion from the crucible and crucible lining during ingot cooling [1], the total iron concentration moving up the ingot becomes limited by the diffusivity of iron. The bright lines in Figures 4 and 5 are caused by surface scratches and represent optical artefacts in the Fe_i images.

In the central part of the ingot, as represented by as-cut wafer 140 in Figure 5, [Fe_i] has dropped significantly compared to the lower part of the ingot (see Figures 1 and 6), as we are now well beyond the region into which iron can diffuse from the crucible during ingot growth. The Fe_i image of as-cut wafer 140 (Figure 5) has a much weaker contrast, indicating a reduced degree of precipitation at the grain boundaries. This is believed to be related to the magnitude of the Fe_i concentration. If the precipitation at grain boundaries is only initiated once the solubility limit of iron is exceeded by the local iron concentration within the grains, then such precipitation will occur at lower temperatures in those parts of the ingot with lower iron concentrations, meaning that the iron will not be as mobile, nor will it be precipitating for as long, leading to a reduced degree of precipitation.

The concentration of Fe_i starts to rise again in the top part of ingot, as illustrated in Figure 1. This can be explained by the effect of segregation during the solidification process [1]. The interstitial iron images of wafers from the top part of the ingot were observed to be qualitatively similar to wafer 140 in Figure 5, although with increased noise, which is believed to be the result of other lifetime-limiting impurities aggregating at the ingot top due to the segregation effect.

3.3. Gettered wafers

The Fe_i images of gettered wafers are shown in Figures 7–9, the first of which received standard gettering and the other two extended gettering. The Figures illustrate a reversed distribution of Fe_i to those of the corresponding adjacent as-cut wafers (Figures 3 and 4), the most striking example being a comparison between Figures 4 and 9. The concentration of Fe_i at grain boundaries and dislocation

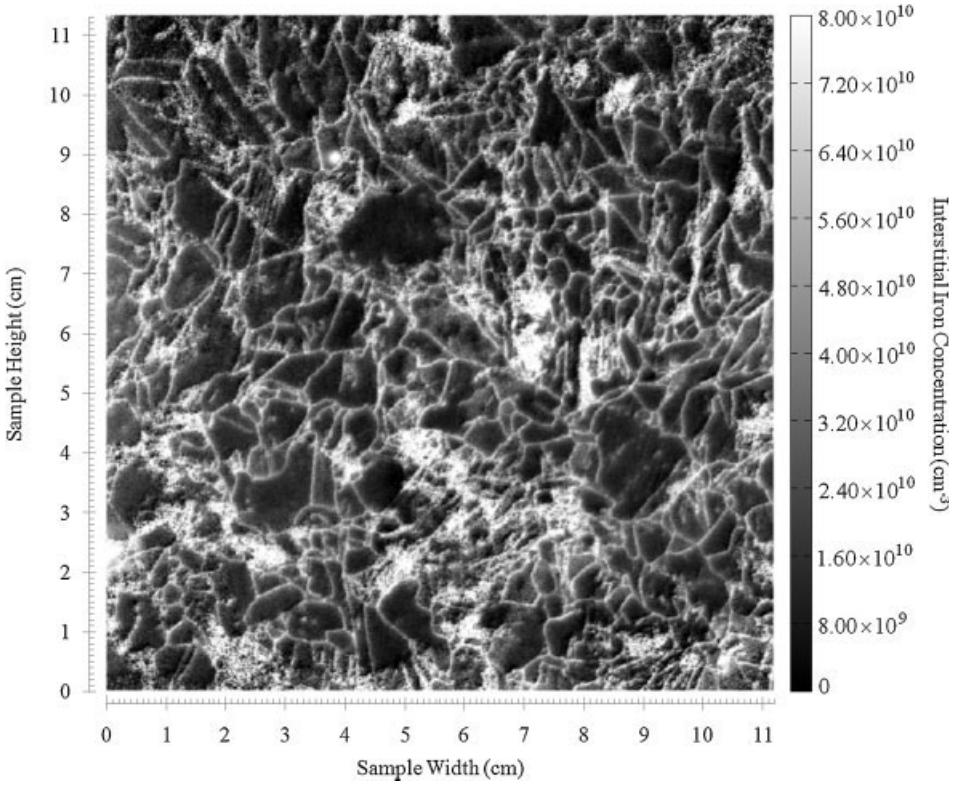

Figure 9. Interstitial iron image of extended gettered wafer 93.

clusters is now higher than inside the grains. Such an effect is expected on the basis of previous modelling [18]. During gettering, the high temperature drives precipitated iron to re-dissolve into the silicon matrix [22], thus increasing Fe_i concentration at grain boundaries and dislocations; meanwhile a large fraction of interstitial iron is gettered, both inside the grains and at grain boundaries. The combined result is a higher $[Fe_i]$ at grain boundaries and dislocation clusters, as has been proposed previously [23].

The Fe_i distribution of standard gettered wafer 70 (Figure 7) uniquely exhibits reduced Fe_i concentrations *near* grain boundaries compared to increased $[Fe_i]$ both inside the grains and at the grain boundaries. A possible explanation is that the precipitated iron at grain boundaries which re-dissolves during gettering and diffuses into the grains, does not extend as far as the width of the denuded regions around the as-cut wafer's grain boundaries, formed as a result of internal gettering during ingot cooling. This occurs because the ingot cooling process has a much larger thermal budget and a much longer time period than the phosphorus gettering. This conjecture is supported by the Fe_i image of the neighbouring wafer 67, which, after an additional 5 h anneal at a slightly lower temperature, exhibits a less abrupt change in $[Fe_i]$ distribution near the grain boundaries, as shown in Figure 8. The reason why this interesting phenomenon is only observed in this part of the ingot is likely to be related to the fact that it has the highest $[Fe_i]$, as evident in Figure 1, causing an earlier onset of precipitation and thus broader denuded regions.

A significant decline in Fe_i concentration is observed in standard gettered wafers compared to as-cut wafers, on the order of one to two magnitudes, as shown in Figure 1. After extended gettering, the Fe_i concentration is further reduced to less than half of that of the standard gettered wafers. The beneficial effect of such extended gettering has been observed previously [24–26]. The reduction in the Fe_i concentration occurs everywhere in the wafer, both inside the grains and at the grain boundaries. The variation in Fe_i concentration from different parts of the ingot drops from two orders of magnitudes in as-cut wafers to one order of magnitude after standard gettering process and becomes even smaller after extended gettering (see Figure 1). A limitation of the technique used is that the Fe_i images become noisier as Fe_i concentration approaches the detection limit in the order of $10^{10}\,cm^{-3}$.

4. CONCLUSION

In this work, we have imaged the interstitial iron distributions across mc-Si wafers by applying the PL imaging technique at low injection levels well below the cross-over point. The results show that the concentration of interstitial iron in the as-cut state first increases rapidly from the bottom to lower-middle part of an ingot, most probably due to reduced precipitation sites related to grain boundaries and intra-grain sites such as oxygen precipitates. It then starts to decline as a result of diffusivity limitation in the central part; and $[Fe_i]$ rises again in the top section of the ingot, owing to segregation during solidification, as has been observed previously. Phosphorus gettering was found to accomplish significant reductions of $[Fe_i]$ in mc-Si, in all parts of the wafers and along all sections of the ingot. A further reduction in $[Fe_i]$ is possible via additional annealing of the diffused wafers. The Fe_i images clearly reveal internal gettering of iron to grain boundaries and dislocation clusters during mc-Si ingot cooling. As precipitated iron re-dissolves during the high-temperature gettering process, the resulting gettered wafers exhibit a reversed distribution of Fe_i at crystallographic defects compared to as-cut wafers.

ACKNOWLEDGEMENTS

This work has been supported by the Australian Research Council. The authors are grateful to Jason Tan for supplying the wafers studied in this work and to Chris Samundsett for assistance with sample preparation.

REFERENCES

1. Macdonald D, Cuevas A, Kinomura A, Nakano Y, Geerligs LJ. Transition metal profiles in a multicrystalline silicon ingot. *Journal of Applied Physics* 2005; **97**: 033523.
2. Buonassisi T, Istratov AA, Pickett MD, Heuer M, Kalejs JP, Hahn G, Marcus MA, Lai B, Cai Z, Heald SM, Ciszek TF, Clark RF, Cunningham DW, Gabor AM, Jonczyk R, Narayanan S, Sauar E, Weber ER. Chemical natures and distributions of metal impurities in multicrystalline silicon materials. *Progress in Photovoltaics: Research and Applications* 2006; **14**: 513.
3. Macdonald D, Tan J, Trupke T. Imaging interstitial iron concentrations in boron-doped crystalline silicon using photoluminescence. *Journal of Applied Physics* 2008; **103**: 073710.
4. Trupke T, Bardos RA, Schubert MC, Warta W. Photoluminescence imaging of silicon wafers. *Applied Physics Letters* 2006; **89**: 044107.
5. Zoth G, Bergholz W. A fast, preparation-free method to detect iron in silicon. *Journal of Applied Physics* 1990; **67**: 6764.
6. Sinton RA, Cuevas A. Contactless determination of current–voltage characteristics and minority-carrier lifetimes in semiconductors from quasi-steady-state photoconductance data. *Applied Physics Letters* 1996; **69**: 2510.
7. Macdonald D, Cuevas A. Trapping of minority carriers in multicrystalline silicon. *Applied Physics Letters* 1999; **74**: 1710.
8. Herlufsen S, Schmidt J, Hinken D, Bothe K, Brendel R. Photoconductance-calibrated photoluminescence lifetime imaging of crystalline silicon. *Physica Status Solidi – Rapid Research Letters* 2008; **2**: 245.

9. Macdonald D, Roth T, Deenapanray PNK, Trupke T, Bardos RA. Doping dependence of the carrier lifetime crossover point upon dissociation of iron–boron pairs in crystalline silicon. *Applied Physics Letters* 2006; **89**: 142107.
10. Geerligs LJ, Macdonald D. Dynamics of light-induced dissociation of FeB pairs in crystalline silicon. *Applied Physics Letters* 2004; **85**: 5227.
11. Schubert MC, Kerler MJ, Warta W. Influence of heterogeneous profiles in carrier density measurements with respect to iron concentration measurements in silicon. *Journal of Applied Physics* 2009; **105**: 114903.
12. Bardos RA, Trupke T, Schubert MC, Roth T. Trapping artifacts in quasi-steady-state photoluminescence and photoconductance lifetime measurements on silicon wafers. *Applied Physics Letters* 2006; **88**: 053504.
13. Tan J. Overcoming performance limitations of multicrystalline silicon solar cells, *PhD thesis*, The Australian National University, 2008.
14. Kittler M, Seifert W, Stemmer M, Palm J. Interaction of iron with a grain boundary in boron-doped multicrystalline silicon. *Journal of Applied Physics* 1995; **77**: 3725.
15. Buonassisi T, Istratov AA, Heuer M, Marcus MA, Jonczyk R, Isenberg J, Lai B, Cai Z, Heald S, Warta W, Schindler R, Willeke G, Weber ER. Synchrotron-based invetigations of the nature and impact of iron contamination in multicrystalline silicon solar cells. *Journal of Applied Physics* 2005; **97**: 074901.
16. Chen J, Yang D, Xi Z, Sekiguchi T. Recombination activity of $\Sigma 3$ boundaries in boron-doped multicrystalline silicon: Influence of iron contamination. *Journal of Applied Physics* 2005; **97**: 033701.
17. Schön J, Habenicht H, Schubert MC, Warta W. Simulation of iron distribution after crystallization of mc silicon. *Solid State Phenomena* 2010; **156–158**: 223.
18. Schön J, Schubert MC, Habenicht H, Warta W. *Proceedings 25th European Photovoltaic Solar Energy Conference, Valencia, Spain* (WIP-Renewable Energies, 2010;).
19. Tan J, Macdonald D, Bennet N, Kong D, Cuevas A, Romijn I. Dissolution of metal precipitates in multicrystalline silicon during annealing and the protective effect of phosphorus emitters. *Applied Physics Letters* 2007; **91**: 043505.
20. Karg D, Pensl G, Schulz M, Hässler C, Koch W. Oxygen-related defect centers in solar-grade, multicrystalline silicon. A reservoir of lifetime killers. *Physica Status Solidi B* 2000; **222**: 379.
21. Hieslmair H, Istratov A, McHugo S, Flink C, Heiser T, Weber E. Gettering of iron by oxygen precipitates. *Applied Physics Letters* 1998; **72**: 1460.
22. Buonassisi T, Istratov AA, Peters S, Ballif C, Isenberg J, Riepe S, Warta W, Schindler R, Willeke G, Cai Z, Lai B, Weber ER. Impact of metal silicide precipitate dissolution during rapid thermal processing of multicrystalline silicon solar cells. *Applied Physics Letters* 2005; **87**(12): 1918.
23. Habenicht H, Riepe S, Schultz O, Warta W. *Proceedings 22nd European Photovoltaic Solar Energy Conference, Milan, Italy* (WIP-Renewable Energies, 2007;), p. 1519.
24. Manshanden P, Geerligs LJ. Improved phosphorus gettering of multicrystalline silicon. *Solar Energy Materials and Solar Cells* 2006; **90**: 998.
25. Krain R, Herlufsen S, Schmidt J. Internal gettering of iron in multicrystalline silicon at low temperature. *Applied Physics Letters* 2008; **93**: 152108.
26. Pickett MD, Buonassisi T. Iron point defect reduction in multicrystalline silicon solar cells. JT Applied Physics Letters 2008; **92**: 122103.